Branching ratio $\Gamma_\alpha/\Gamma_\gamma$ of the 4.033 MeV $3/2^+$ state in ^{19}Ne

K. E. Rehm, A. H. Wuosmaa,* C. L. Jiang, J. Caggiano,† J. P. Greene, A. Heinz,† D. Henderson, R. V. F. Janssens, E. F. Moore, G. Mukherjee, R. C. Pardo, T. Pennington, J. P. Schiffer, and R. H. Siemssen‡
Argonne National Laboratory, Argonne, Illinois 60439, USA

M. Paul
Hebrew University, Jerusalem, Israel

L. Jisonna and R. E. Segel
Northwestern University, Evanston, Illinois 60208, USA

(Received 14 March 2003; published 30 June 2003)

The branching ratio $\Gamma_\alpha/\Gamma_\gamma$ of the 4.033 MeV $3/2^+$ state in ^{19}Ne plays a crucial role in the breakout from the hot CNO cycle into the rapid proton capture process. This ratio has been studied by making use of the advantages of inverse kinematics. The state was populated via the ^{3}He(^{20}Ne,α)^{19}Ne* reaction and its decay via γ or α emission was measured by detecting the heavy reaction products (^{19}Ne or ^{15}O) in coincidence in a magnetic spectrograph. An upper limit $\Gamma_\alpha/\Gamma_\gamma \leq 6\times10^{-4}$ has been obtained. With these results, the astrophysical reaction rate for the ^{15}O (α,γ) ^{19}Ne reaction has been calculated. Its influence on the breakout at various astrophysical sites, novas, x-ray bursts, and supermassive stars, is discussed.

DOI: 10.1103/PhysRevC.67.065809 PACS number(s): 26.50.+x, 25.55.Hp, 27.20.+n

I. INTRODUCTION

At astrophysical sites where explosive hydrogen burning [1] can occur, e.g., in novas, on accreting neutron stars or in supermassive stars, the energy production at elevated temperatures ($T \geqslant 10^8$ K) proceeds via the so-called hot CNO (HCNO) cycle. This is a reaction cycle consisting of a sequence of (p,γ), (p,α) reactions and β^+ decays: ^{12}C$(p,\gamma)^{13}$N$(p,\gamma)^{14}$O$(e^+\nu_e)^{14}$N$(p,\gamma)^{15}$O$(e^+\nu_e)$ ^{15}N$(p,\alpha)^{12}$C. In this network, the rate of energy production is limited by the slow β decays of ^{14}O and ^{15}O, with $T_{1/2}$ = 70.6 s and 123 s, respectively. At even higher temperatures ($T \geqslant 3.5\times10^8$ K), α-induced reactions on ^{14,15}O can bypass these waiting points, resulting in a strong increase in the energy production rate and, possibly, in the breakout from the HCNO cycle into the rapid proton capture (rp) process, where, through a sequence of (p,γ) reactions and β^+ decays, nuclei above mass 20 are produced [2].

Once elements heavier than ^{19}Ne are formed, the reaction Q values in this mass region are such that no reaction sequence can recycle the nuclei back into CNO material. There are three possible breakout pathways from the CNO cycles into the rp process: ^{18}F$(p,\gamma)^{19}$Ne, ^{15}O$(\alpha,\gamma)^{19}$Ne, and ^{18}Ne$(\alpha,p)^{21}$Na. The first path, ^{18}F(p,γ), requires the production of ^{18}F which can occur either via the ^{16}O$(p,\gamma)^{17}$F$(p,\gamma)^{18}$Ne$(\beta^+\nu_e)^{18}$F route or through the sequence ^{14}O$(\alpha,p)^{17}$F$(p,\gamma)^{18}$Ne$(\beta^+\nu_e)^{18}$F. The first route is hampered by the small cross section characterizing the ^{16}O$(p,\gamma)^{17}$F reaction [3,4] while, for the second reaction, the small yield for the ^{14}O$(\alpha,p)^{17}$F reaction is the main bottleneck [5–7]. Furthermore, the positive Q value for the ^{18}F$(p,\alpha)^{15}$O reaction leads to a very small value for $\Gamma_\gamma/\Gamma_\alpha$ [8] and, thus, to a negligible breakout probability through ^{18}F. The third path, ^{18}Ne$(\alpha,p)^{21}$Na, has the highest Coulomb barrier of the three breakout reactions and is, thus, thought to contribute only at higher temperatures and densities [9]. It is presently assumed [1] that the ^{15}O(α,γ) reaction is the most likely path for the breakout from the HCNO cycle into the rp process.

A direct measurement of the ^{15}O$(\alpha,\gamma)^{19}$Ne reaction, which has an estimated cross section of $\sim$100 pb, is currently not feasible because it requires very intense ^{15}O beams that are not yet available [10]. For this reason, only indirect measurements have been performed so far.

The portion of the level scheme of ^{19}Ne relevant for the ^{15}O(α,γ) reaction is presented in Fig. 1 [11]. The first states in ^{19}Ne above the (α,γ) threshold at 3.529 MeV are a $3/2^+$ state at 4.033 MeV, followed by $9/2^-$ and $7/2^-$ levels at

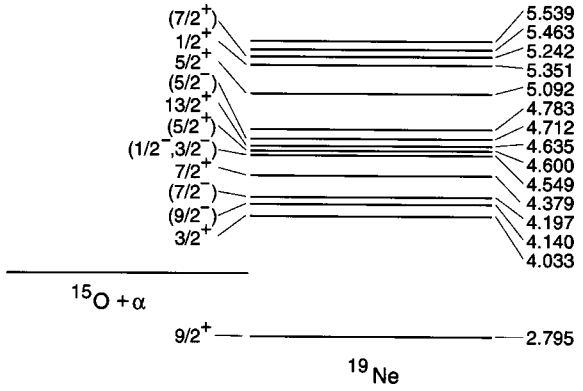

FIG. 1. Level scheme of ^{19}Ne in the vicinity of the (α) threshold.

*Present address: Department of Physics, Western Michigan University, Kalamazoo, MI 49008.

†Present address: Wright Nuclear Structure Laboratory, Yale University, New Haven, CT 06520.

‡Present address: Kernfysisch Versneller Instituut, Groningen, The Netherlands.

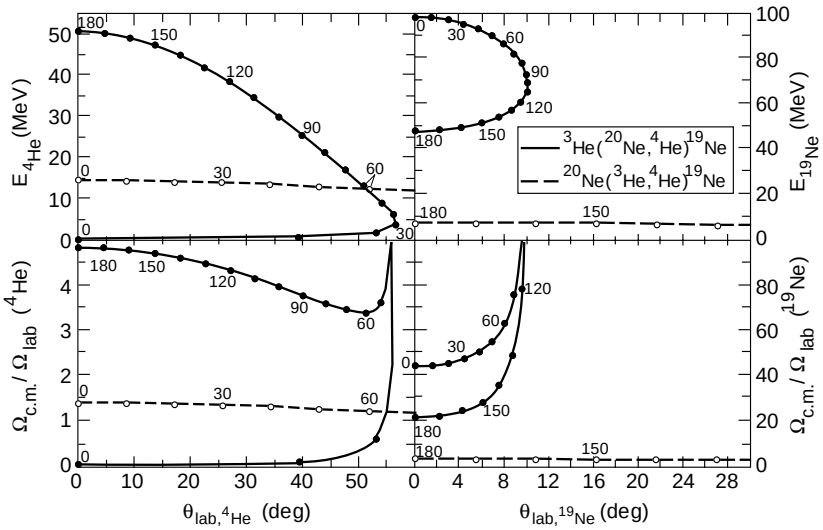

FIG. 2. Comparison of the kinematics for the ^{3}He(^{20}Ne,α)^{19}Ne (solid lines) and ^{20}Ne(^{3}He,α)^{19}Ne reactions (dashed lines). The numbers next to the solid points indicate the c.m. angles. (a) E_{lab}(^{4}He) vs θ_{lab}(^{4}He), (b) E_{lab}(^{19}Ne) vs θ_{lab}(^{19}Ne), (c) ratio of solid angles $\Omega_{\text{c.m.}}/\Omega_{lab}$ for detecting ^{4}He, (d) same as (c) but for ^{19}Ne.

4.140 and 4.197 MeV, respectively. Because of the small angular momentum transfer ($\Delta l=1$) and the lower excitation energy, the $3/2^+$ level is expected to dominate the (α,γ) reaction rate. The contributions from the next two levels are suppressed by about an order of magnitude due to the larger angular momentum transfer ($\Delta l=4$).

In Ref. [12] an estimate of the (α,γ) reaction rate was obtained through a measurement of the spectroscopic factor of the $3/2^+$ state in the mirror nucleus ^{19}F, populated via the ^{15}N(^{6}Li,d)^{19}F reaction. From this measurement, an α width, $\Gamma_\alpha=9\ \mu$eV, was deduced. Together with $\Gamma_\gamma=73\pm41$ meV, again taken from the decay in the mirror nucleus ^{19}F [11], an estimated branching ratio of $\Gamma_\alpha/\Gamma_\gamma\sim10^{-4}$ was obtained. As outlined in Ref. [13], however, estimates based on analog states can be quite uncertain and, thus, experiments that can obtain direct information of the α width for the $3/2^+$ state in ^{19}Ne are needed. Due to the small value of Γ_α, however, these measurements are very difficult.

In the indirect measurements reported so far, the $3/2^+$ state in ^{19}Ne was populated in a transfer reaction and the branching ratio of the subsequent decay of ^{19}Ne into α and ^{15}O was determined. Possible transfer reactions include ^{19}F(^{3}He,t) [14,15], ^{18}Ne(d,p) [16], ^{20}Ne(d,t) [15], ^{20}Ne(^{3}He,α) [17], ^{12}C(^{11}C,α) [18], ^{12}C(^{17}O,^{10}Be) [19], and ^{21}Ne(p,t) [20]. While earlier attempts [14,15] have used normal kinematics, e.g., bombarding a ^{19}F target with a ^{3}He beam, a large increase in the efficiency for detecting ^{19}Ne and its decay products (^{15}O$+\alpha$) can be achieved by taking advantage of inverse kinematics, i.e., bombarding a ^{3}He target with a ^{19}F beam. Under these conditions, the ^{19}Ne nuclei produced in the reaction are focused into a small forward cone yielding an improvement in the detection efficiency by a factor of more than 10. The advantages of inverse kinematics are illustrated in Fig. 2 for the example of the reaction ^{20}Ne(^{3}He,α)^{19}Ne ($E_x=4.033$ MeV) performed at the same center-of-mass (c.m.) energy ($E_{\text{c.m.}}=13$ MeV) with either a ^{3}He beam bombarding a ^{20}Ne target or with a ^{20}Ne beam bombarding a ^{3}He target. A ^{3}He beam results in high-energy α particles that can be easily detected with solid state detectors or a magnetic spectrograph (see dashed line in Fig. 2). The energies of the corresponding ^{19}Ne particles are, however, below 4 MeV, i.e., too low to escape from a ^{20}Ne gas target. In addition, the α particles from the decay of the 4.033-MeV state in ^{19}Ne are then emitted over the full solid angle and with very low energies, requiring a large-area Si detector array for good detection efficiency.

The case for inverse kinematics with a ^{20}Ne beam is represented by the solid lines in Fig. 2. Because of the high c.m. momentum in the laboratory system, the α and ^{19}Ne particles are restricted to a forward cone with opening angles of 56.7° and 10.1°, respectively. α particles emitted at small c.m. angles [21] emerge at forward laboratory angles with very low energies. As a result, only particles in the range $\theta_{\text{c.m.}}\geqslant 30°$ have energies that are sufficient to be detectable by standard techniques. The corresponding ^{19}Ne particles are emitted into a small forward cone with typical energies of 2–5 MeV/nucleon. When ^{19}Ne decays in flight the decay products (α and ^{15}O) have then comparable velocities. These high recoil velocities make it possible to directly detect and identify the ^{15}O nuclei that are produced with much smaller yields than the α particles arising from a variety of background reactions such as ^{20}Ne breakup. Because of the forward focusing, the ratio of the solid angles $\Omega_{\text{c.m.}}/\Omega_{lab}$, shown in the lower part of Fig. 2, is larger in inverse kinematics by factors of about 4 (for ^{4}He detection) and 10 (for ^{19}Ne detection). Detecting the heavy reaction product ^{15}O from the decay of ^{19}Ne works especially well for states in the vicinity of the threshold, which are states that play a dominant role in astrophysical applications. Furthermore, since the opening cone for the decay of ^{19}Ne into ^{15}O$+\alpha$ decreases with increasing ^{19}Ne velocities, higher bombarding energies are clearly advantageous. Thus, the ratio of the number of ^{15}O and ^{19}Ne events, detected in kinematic coincidence with α particles populating the $3/2^+$ state at 4.033 MeV, directly measures the branching ratio $\Gamma_\alpha/\Gamma_\gamma$. A similar technique has been used previously for a measurement of the branching ratio $\Gamma_\gamma/\Gamma_{total}$ [22]. In this case, however, the mass and Z of the heavy reaction product were not identified and, therefore, only branching ratios greater than $\sim$0.1 could

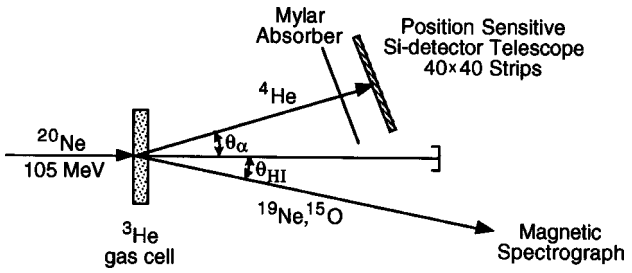

FIG. 3. Schematic representation of the experimental setup. The ^{3}He cell has 1.5-mg/cm^2-thick Ti entrance and exit windows. See text for a detailed description.

be determined. This is not sufficient for ^{19}Ne, where a considerably higher level of sensitivity is needed.

II. EXPERIMENTAL DETAILS

There are several good candidates among the possible transfer reactions that can populate the 4.033 MeV $3/2^+$ state in ^{19}Ne. One of these is the $p(^{21}\mathrm{Ne},^{19}\mathrm{Ne})t$ reaction [23] which, because of its large negative Q value ($Q=-19.177$ MeV), requires a ^{21}Ne beam with an energy of at least 20 MeV/nucleon. This energy is beyond the present capabilities of ATLAS and has therefore been investigated elsewhere [20].

We have studied the $d(^{20}\mathrm{Ne},^{19}\mathrm{Ne})t(Q=-14.641$ MeV) and $^3\mathrm{He}(^{20}\mathrm{Ne},^{19}\mathrm{Ne})\alpha(Q=-0.320$ MeV) reactions, using a solid CD_2 target or a gas cell filled with D_2 or ^{3}He gas. For the $d(^{20}\mathrm{Ne},t)^{19}$Ne reaction the cross section for populating the $3/2^+$ level was found to be only of the order of 20 μb/sr with comparable yields for the neighboring $7/2^-$ and $9/2^-$ states [15]. Similar results are found for the $^3\mathrm{He}(^{19}\mathrm{F},t)^{19}$Ne reaction ($Q_{\mathrm{g.s.}}=-3.258$ MeV) which more favorably populates the neighboring $7/2^-$ and $9/2^-$ states [14,15]. In a high-resolution study of the $^{20}\mathrm{Ne}(^3\mathrm{He},\alpha)^{19}$Ne reaction at $E_{lab}=15$ MeV using a magnetic spectrograph it was shown [17] that, in the angular region $\theta_{\mathrm{c.m.}}\geqslant 30°$ (where, in an experiment in inverse kinematics, the α particles have high enough energies), the cross sections are typically around 100 μb/sr. We have, therefore, chosen to study the inverse reaction $^3\mathrm{He}(^{20}\mathrm{Ne},\alpha)^{19}$Ne at the same c.m. energy, using a ^{20}Ne beam of $\sim$105 MeV

The different magnetic rigidities of the reaction products α, ^{19}Ne, and ^{15}O permit their spatial separation at 0° in the focal plane of a large-acceptance Enge split-pole spectrograph. It was discovered, however, that energy and small-angle straggling of the primary ^{20}Ne beam in the ^{3}He gas cell resulted in a high background rate restricting the primary beam intensity to less than 0.1 pnA, which is too low for a measurement of $\Gamma_\alpha/\Gamma_\gamma$ below 10^{-3}. The magnetic spectrometer was consequently rotated away from 0° to an angle of 3.7°.

A schematic representation of the experimental arrangement used in this work is shown in Fig. 3. The ^{20}Ne beam bombarded a 1.5-mm-long gas cell filled with ^{3}He at 700 mbar. The entrance and exit windows of the cell consisted of 1.5-mg/cm^2 titanium foils. The gas target was cooled to liquid nitrogen temperature, resulting in a ^{3}He thickness of 50 μg/cm^2. The pressure in the ^{3}He target was kept constant to better than 1%. For an incident 104.8-MeV ^{20}Ne beam, the energy in the center of the target was 98.3 MeV. The ^{20}Ne beam intensity was approximately 1 pnA. In order to minimize the effects of kinematic broadening, the beam spot on the ^{3}He target was collimated to a diameter of 1 mm.

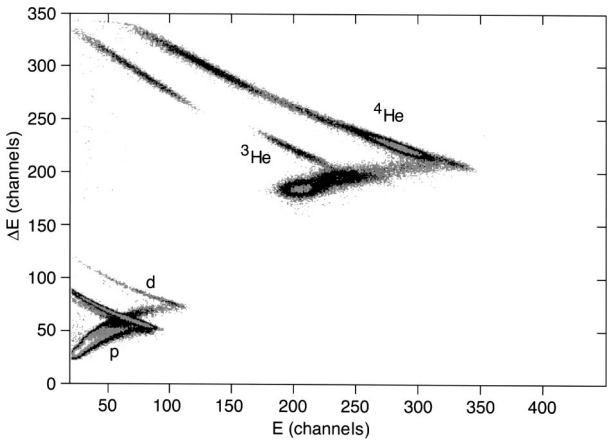

FIG. 4. ΔE-E_{res} spectrum for light particles measured with the Si detector telescope.

The outgoing α particles from the $^3\mathrm{He}(^{20}\mathrm{Ne},\alpha)^{19}$Ne reaction were detected in a Si strip detector telescope consisting of a 500-μm-thick, 40×40 mm^2 ΔE detector backed by a 50×50 mm^2, 300-μm-thick E_{res} detector tilted by an angle of 50° in order to increase its effective thickness for the incident particles to about 500 μm. The ΔE detector was subdivided in the front and back into 32 vertical and horizontal strips (1-mm width) which were read out individually. The telescope was calibrated using a ^{228}Th α source and energy resolutions of 45 keV for the ΔE and E_{res} detectors were obtained. The Si detector telescope covered a solid angle of about 35 msr in the angular range $\theta_{\mathrm{c.m.}}=6.8°-17.2°$. A 29.6-mg/cm^2-thick Mylar absorber was mounted directly in front of the ΔE detector in order to stop ^{20}Ne particles elastically scattered from the entrance or exit foils of the gas target. A two-dimensional ΔE-E_{res} spectrum, measured with the ^{3}He target, is presented in Fig. 4. Regions corresponding to protons, deuterons, ^{3}He, and ^{4}He particles are clearly visible in the spectrum. Because of its total thickness of only 1000 μm, higher energy particles were not stopped in the telescope, leading to the characteristic kinks in the light-particle distributions shown in Fig. 4. For the α channel, this affected only α particles from the $^3\mathrm{He}(^{20}\mathrm{Ne},\alpha)^{19}$Ne reaction populating states below an excitation energy of about $E_x=2.8$ MeV in ^{19}Ne. The α particles populating states in the energy region above the (α,γ) threshold at $E_x=3.529$ MeV were all stopped in the E_{res} detector.

The energy resolution that can be achieved with this setup is determined by many contributions, including the geometries of the detector and the ^{3}He target, the energy and angle straggling in the window foils of the gas target, and the intrinsic resolution of the detector. These individual contributions are summarized in Table I. Adding these in quadrature results in a 385-keV value for the energy resolution. This

TABLE I. Contributions to the energy resolution of α particles measured in the Si ΔE-E telescope.

Source	Uncertainty (keV)
Pixel resolution	175
Angle uncertainty due to beam spot diameter	125
Angle uncertainty due to finite length of the target	35
Small angle straggling of ^{4}He in Ti exit foil	80
Energy loss straggling of ^{4}He in Ti exit foil	20
Small angle straggling of ^{4}He in Mylar foil	110
Energy loss straggling of ^{4}He in Mylar foil	70
Energy loss and straggling of ^{20}Ne in Ti foil and ^{3}He target	270
Intrinsic energy resolution of Si detector and electronics	65
Total	385

translates into a Q value resolution of about 210 keV, in good agreement with the experimental resolution of 220 keV. The main contribution to the energy resolution comes from the relatively large energy loss of ^{20}Ne in the 50-μg/cm^2 ^{3}He target. This resolution could be improved by running the gas cell at a lower pressure, but the reduced target thickness would require correspondingly longer running times.

The heavy reaction products (e.g., ^{19}Ne, ^{15}O, ^{18}F) from the ^{3}He(^{20}Ne,α) reaction were separated according to their magnetic rigidities in the Enge split-pole spectrograph. Mass m, nuclear charge Z, and magnetic rigidity information were provided by a hybrid, position-sensitive heavy ion focal-plane detector consisting of a multiwire parallel-plate counter filled with 5 Torr of isobutane, providing position and time information. This was followed by a Bragg-curve-type ionization chamber with CF_4 as the counter gas for a measurement of energy E, nuclear charge Z, and particle range [26]. In order to cover the full range in energy and Z of the outgoing particles, a pressure of 35 Torr was chosen for the ionization chamber. Figure 5 presents spectra of particle range versus E^2 measured for heavy particles emitted in the angular range $\theta_{lab}=3.7°\pm1.4°$ coincident with an α particle detected in the Si telescope (see Fig. 4). The groups corresponding to Ne, F, and O are indicated. High-energy oxygen particles are not stopped in the detector and, therefore, the O line reaches a maximum value in E^2 before bending backward around channel 250. Events with nuclear charges $Z=8-10$, selected from Fig. 5, are shown separately in a two-dimensional plot of time-of-flight (TOF) versus magnetic rigidity $B\rho$ and E versus $B\rho$ in the top and bottom panels of Fig. 6, respectively. The groups corresponding to different charge states q and masses m are also indicated in the figure. From these two plots, particles with different m/q values can be selected. The mass m is, thus, determined by

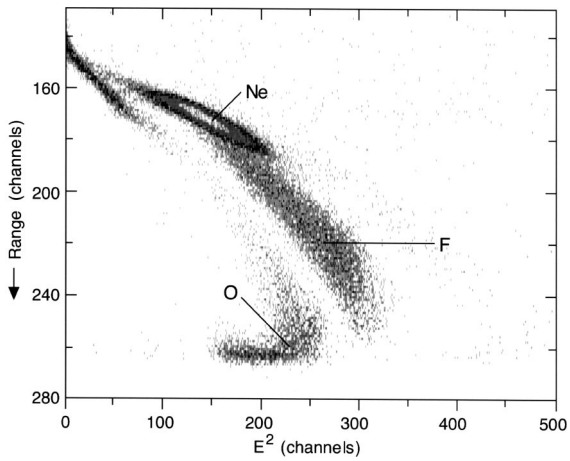

FIG. 5. Particle identification spectrum (range vs E^2) for heavy particles measured with the Bragg-ionization chamber in the focal plane of the Enge split-pole spectrograph.

two independent measurements (energy and TOF). The nuclear charge Z can also be determined from two independent measurements, either from a plot of range versus E^2 (see Fig. 5) or from the height of the Bragg peak (see Ref. [26] for details). The redundant determination of the two critical parameters Z and m, therefore, provides a high degree of background suppression.

The experimental setup was tested by studying elastic and inelastic scattering of α particles from ^{20}Ne at backward angles [24]. Similar to the case of ^{19}Ne, excited states in ^{20}Ne above an excitation energy $E_x=4.729$ MeV can decay via α emission to the ground state of ^{16}O. Since this is a well studied system [25], it served as a convenient calibration reaction.

III. EXPERIMENTAL RESULTS

The nucleus ^{19}Ne becomes particle unbound with respect to α emission at an excitation energy of 3.529 MeV, and with respect to proton emission at 6.410 MeV. Thus, α particle spectra measured by the Si detector telescope in coincidence

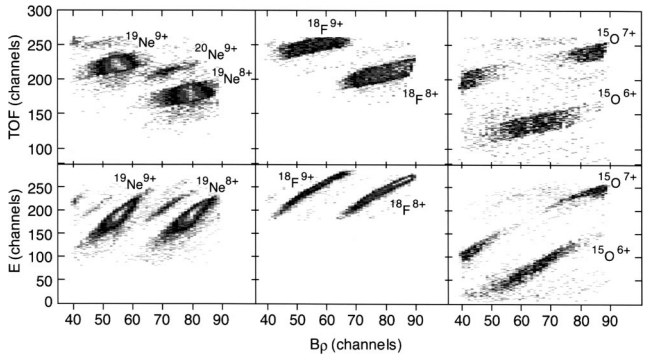

FIG. 6. Top: Two-dimensional plots of TOF vs magnetic rigidity $B\rho\sim p/q$ for Ne, F, and O particles selected from the particle identification spectrum shown in Fig. 5. Bottom: Two-dimensional plots of E vs $B\rho$ for Ne, F, and O particles. The mass and charge values of the different particle groups are indicated.

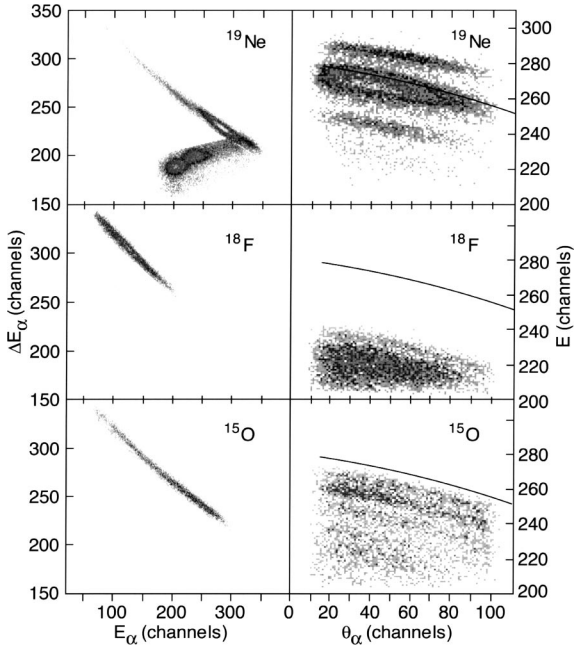

FIG. 7. Left: ΔE-E spectra for α particles in coincidence with ^{19}Ne, ^{18}F, and ^{15}O, respectively, selected from the particle groups shown in Fig. 6. Right: Two-dimensional spectra of E_α vs θ_{lab} for α particles in coincidence with ^{19}Ne, ^{18}F, and ^{15}O. For ^{19}Ne, the α spectrum has been restricted to particles stopped in the ΔE-E telescope. The solid lines represent the kinematic location of the 4.033-MeV state in ^{19}Ne.

with ^{15}O or ^{18}F particles should not extent beyond these excitation energies, while α particles coincident with ^{19}Ne can populate all states. This is confirmed by the Si telescope spectra shown in the left part of Fig. 7 plotted in the ΔE-E_{res} plane. As discussed above, α particles populating states in ^{19}Ne below $E_x = 2.8$ MeV are too energetic to be fully stopped in the Si telescope. The right part of Fig. 7 gives two-dimensional spectra of E versus Θ_{lab} ($E = \Delta E + E_{res}$) for α particles detected in the Si telescope in coincidence with ^{19}Ne, ^{15}O, and ^{18}F, respectively, detected in the magnetic spectrograph. The scattering angle was calculated from the geometry of the individual pixels of the Si strip detector. The kinematic curves expected for the 4.033 MeV state are indicated by solid lines.

When ^{19}Ne decays in flight into ^{15}O$+\alpha$ or into ^{18}F$+p$, the ^{15}O or ^{18}F nuclei are emitted with respect to the original ^{19}Ne direction within cones whose opening angles increase with increasing ^{19}Ne excitation energy. Because the spectrograph has a finite entrance aperture, only a part of these cones will be accepted and transmitted to the focal plane detector. The relative acceptances have been calculated using Monte Carlo simulations that take into account the kinematics of the reaction, small angle scattering in the foils of the gas target, as well as the charge state distributions. As an example, the efficiency ratio $\epsilon(^{19}\text{Ne})/\epsilon(^{15}\text{O})$ is plotted in Fig. 8 as a function of excitation energy in ^{19}Ne. The rise in $\epsilon(^{19}\text{Ne})/\epsilon(^{15}\text{O})$ towards higher excitation energies originates from the increase of the opening angle for the decay of ^{19}Ne into ^{15}O$+\alpha$. For the first state above the α threshold at E_x

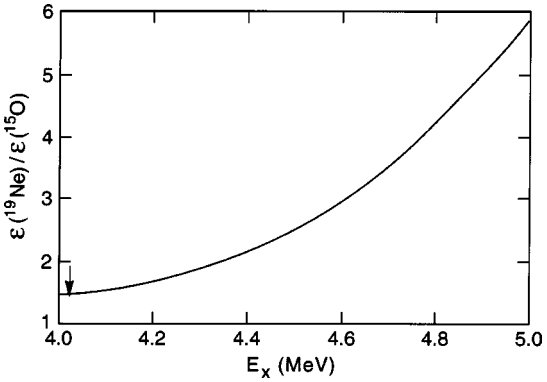

FIG. 8. Relative efficiency $\epsilon(^{19}\text{Ne})/\epsilon(^{15}\text{O})$ for detecting ^{19}Ne or ^{15}O in the focal plane of the magnetic spectrograph. The arrow indicates the location of the 4.033-MeV state.

$=4.033$ MeV, this efficiency correction is about 1.4. A factor of 1.2 is caused by the charge state distribution while the rest is due to the geometrical acceptance of ^{19}Ne and ^{15}O, respectively. For the geometrical acceptance the α particle was assumed to be emitted isotropically in the ^{19}Ne rest frame. A $[1+3\cos^2(\theta)]/2$ distribution results in a 10% decrease of $\epsilon(^{19}\text{Ne})/\epsilon(^{15}\text{O})$ for the 4.033-MeV state. The total uncertainty for $\epsilon(^{19}\text{Ne})/\epsilon(^{15}\text{O})$ is about 20%.

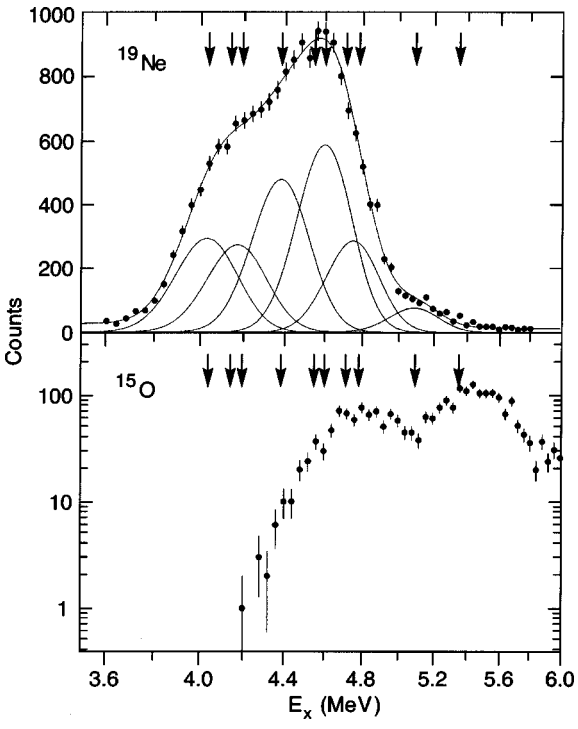

FIG. 9. Excitation energy spectra for α particles in coincidence with ^{19}Ne (top) or ^{15}O (bottom). The solid lines in the ^{19}Ne spectrum are the result of a deconvolution into Gaussian peaks located at excitation energies taken from Ref. [17]. The arrows indicate the locations of the known levels in ^{19}Ne.

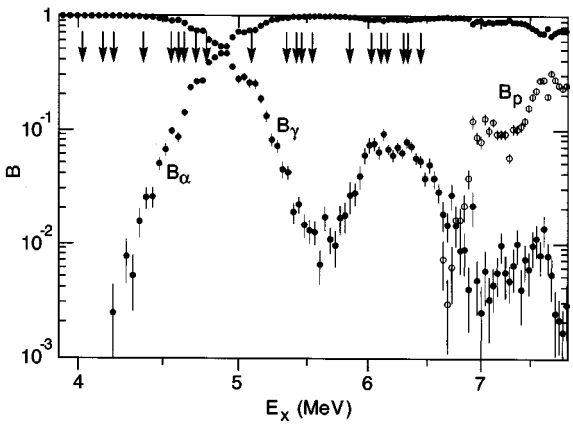

FIG. 10. Branching ratios B_γ, B_α, and B_p, calculated from the efficiency-corrected ^{19}Ne, ^{15}O, and ^{18}F spectra, as a function of the excitation energy in ^{19}Ne. The arrows indicate the location of the known levels in ^{19}Ne.

The ^{19}Ne excitation energy spectra, derived from the measured α-particle energy and angle appear in Fig. 9 for α particles in coincidence with ^{19}Ne and ^{15}O, respectively. The ^{19}Ne coincidence spectrum has been deconvoluted with a least-squares fit into contributions from individual states (see Fig. 1) indicated by Gaussian curves, superimposed on a linear background. This background is caused by tails from incompletely stopped α particles (see Fig. 7) populating states of lower excitation energy in ^{19}Ne. The location of the peaks was kept fixed at the excitation energies obtained in the high-resolution ^{20}Ne(^{3}He,α)^{19}Ne experiment of Ref. [17]. In order to reduce the number of parameters in the fit, states separated by less than 100 keV in excitation energy were combined into a single peak. The yield for populating the 4.033-MeV state is deduced from this spectrum. In the corresponding ^{15}O coincidence spectrum no events were observed for the 4.033-MeV state during a 3.5 day long experiment. Including the efficiency correction from Fig. 8, and using the statistical formulas based on a Bayesian statistical analysis of Ref. [27] an upper limit (90% confidence limit) of 7×10^{-4} for the branching ratio Γ_α/Γ is obtained. Adding the results obtained in a test run, where an annular position-sensitive Si detector replaced the ΔE-E telescope, the upper limit for the branching ratio becomes 6×10^{-4}. This upper limit is comparable with the results obtained recently [20] using the $p(^{21}\mathrm{Ne},t)^{19}$Ne reaction. The inverse (p,t) reaction has a large cross section for populating the 4.033 MeV $3/2^+$ state [23]. On the other hand, the higher bombarding energy ($\sim$40 MeV/nucleon) also resulted in a higher ^{15}O background, due to fragmentation of the incident ^{21}Ne beam.

Because of the Q-value resolution ($\Delta Q\sim220$ keV) and the increasing level density, it is difficult to extract branching ratios for higher-lying states. In Fig. 10, we have, therefore, plotted the ratios of the spectra ^{19}Ne/Σ, ^{15}O/Σ, and ^{18}F/Σ, where Σ is the sum of the efficiency-corrected ^{19}Ne, ^{15}O, and ^{18}F counts. This spectrum gives a measure of the energy-averaged branching ratios Γ_γ/Γ, Γ_α/Γ, and Γ_p/Γ. The arrows indicate the locations of known states in ^{19}Ne. The only levels that are sufficiently well separated from their neighbors are the 5.092-MeV state and, to a lesser extent, the 4.379-MeV state. For these two levels, branching ratios $\Gamma_\alpha/\Gamma=0.8\pm0.1$ (5.092 MeV) and 0.016 ± 0.005 (4.379 MeV) are obtained. These values are in good agreement with the results reported in Refs. [14,20] (see Table II).

In Fig. 10, one observes an increase in Γ_γ/Γ at excitation energies above 6 MeV and 7 MeV, indicating that there are states in this excitation energy region decaying with $\sim$10% probability via γ emission. These are probably high-spin states (e.g., $7/2^-$, $9/2^+$, $11/2^-$) in analogy with similar levels observed in this energy range in the mirror nucleus ^{19}F [22] with Γ_γ/Γ branching ratios between 2 and 20 %. Because of the high level density, however, no spin assignments are proposed.

IV. ASTROPHYSICAL IMPLICATIONS

For a calculation of the astrophysical reaction rate, values for the resonance strengths

TABLE II. Excitation and resonance energies, spin parities, branching ratios, γ widths, and resonance strengths for states in ^{19}Ne above the α threshold at $E_x=3.529$ MeV.

E_x (MeV)	E_r (MeV)	J^π	B_α [a]	B_α [b]	B_α [c]	Γ_γ (meV)	$\omega\gamma$ (meV)
4.033	0.504	$3/2^+$	$<6\times10^{-4}$	$<4.3\times10^{-4}$		$12\pm^{9}_{5}$	2.5×10^{-2}
4.140	0.611	$9/2^-$					5.7×10^{-4} [d]
4.197	0.668	$7/2^-$					8.9×10^{-3} [d]
4.379	0.850	$7/2^+$	0.016 ± 0.005	$<3.9\times10^{-3}$	0.044 ± 0.032	458 ± 92	29 ± 11
4.549	1.020	$3/2^-$		0.16 ± 0.04	0.07 ± 0.03	$39^{+34}_{-1.5}$	$4^{+3.5}_{-1.5}$
4.600	1.071	$5/2^+$		0.32 ± 0.04	0.25 ± 0.04	101 ± 55	90 ± 50
4.712	1.183	$5/2^-$		0.85 ± 0.04	0.82 ± 0.15	43 ± 8	110 ± 21
5.092	1.563	$5/2^+$	0.8 ± 0.1	0.90 ± 0.06	0.90 ± 0.09	196 ± 39	530 ± 110

[a]This work.
[b]Reference [20].
[c]Reference [14].
[d]Calculated assuming spectroscopic factors of 0.1 for the α width.

$$\omega\gamma = \frac{(2J+1)}{(2j_1+1)(2j_2+1)}\frac{\Gamma_\alpha\Gamma_\gamma}{\Gamma_{total}} = \frac{(2J+1)}{(2j_1+1)(2j_2+1)}B_\alpha\Gamma_\gamma \quad (1)$$

are needed. In Eq. (1) J, j_1, and j_2 are the spins of the resonance and of the particles in the incoming channel, respectively. B_α is the α-particle branching ratio and Γ_γ is the γ decay width. Presently no good experimental data are available for Γ_γ for any of the resonances in ^{19}Ne. We have, therefore, used results obtained either from the decay in the mirror nucleus ^{19}F or from theoretical calculations. Values for the widths Γ_γ (see Ref. [20]) and the resulting resonance strengths $\omega\gamma$ are included in Table II. Even with these restrictions, some conclusions regarding the astrophysical implications for the breakout from the hot CNO cycle into the rp process can be drawn from the present measurement.

Although there are ten states in ^{19}Ne in a 1.5-MeV wide window above the α threshold, only two of them play a dominant role for the astrophysical reaction rate calculated via the equation

$$N_A\langle\sigma v\rangle = 1.54\times10^5(AT_9)^{-3/2}\sum_r(\omega\gamma)_r \times\exp(-11.605E_r/T_9), \quad (2)$$

where A is the reduced mass in atomic mass units, T_9 is the temperature in 10^9 K, $\omega\gamma$ the resonance strength in eV, and E_r the resonance energy in MeV. The reaction rate depends linearly on the resonance strength, but exponentially on the resonance energy.

Because of its low energy and low spin value ($3/2^+$), the 4.033-MeV state is expected to dominate the rate at the lowest temperatures. Two suggested values for $\Gamma_\gamma(4.033)$ are published in the literature. In Ref. [14], the value observed for the corresponding transition in the mirror nucleus ^{19}F, $\Gamma_\gamma = 73\pm41$ meV, was used while, in a recent experiment, a value of $12\pm^9_5$ meV was obtained [28]. The latter result has been deduced from the limits provided by lifetime and DSAM measurements including a theoretical value for the $E2/M1$ mixing ratio [28]. The experimental data alone allow values of Γ_γ between 6 and 400 meV. For the calculation we have used the upper limit for Γ_γ (21 meV) from Ref. [28] to obtain a limit of 25 μeV for the resonance strength $\omega\gamma$ (4.033 MeV). The contribution of this state to the astrophysical reaction rate is shown by the solid line in Fig. 11(a). In the temperature range typical of novas ($T_9\sim0.1$–0.4), the $3/2^+$ state dominates the reaction rate by three to four orders of magnitude.

The next two states at $E_x = 4.140$ and 4.197 MeV have tentative spin assignments of $7/2^-$ and $9/2^-$, respectively, and can be populated in the ^{15}O(α,γ) reaction through a $l=4$ transfer. Assuming rather large spectroscopic factors $\theta^2=0.1$, resonance strengths of 0.57 μeV and 8.9 μeV are obtained, which are still considerably smaller than the upper limit obtained for the 4.033-MeV state.

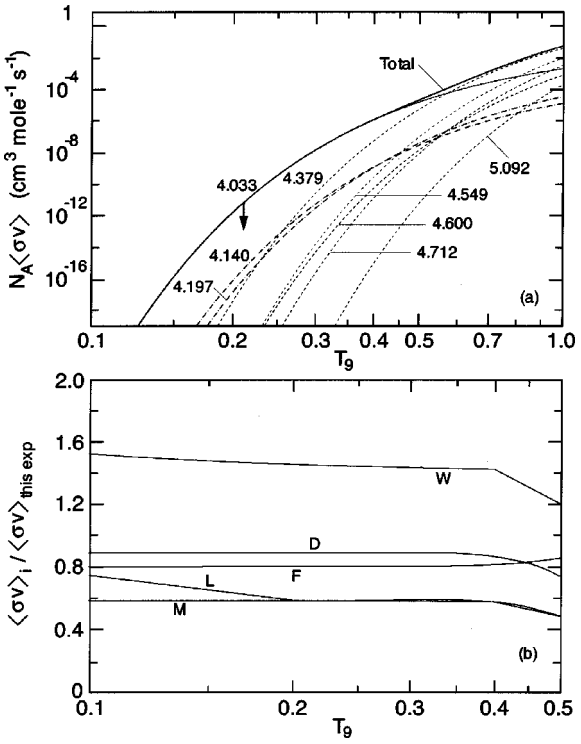

FIG. 11. (a) Astrophysical reaction rate of the ^{15}O$(\alpha,\gamma)^{19}$Ne reaction (solid line) as a function of the temperature in 10^9 K. The contributions from the individual states in ^{19}Ne are indicated in the figure. (b) Ratio of the astrophysical reaction rates taken from the literature and the rate shown in (a) plotted as a function of T_9. W, Ref. [30]; D, Ref. [20]; F, Ref. [12]; L, Ref. [29]; M, Ref. [14].

The next important state for the astrophysical reaction rate is the $7/2^+$ level at 4.379 MeV, which dominates the reaction rate above $T_9=0.6$. For this state two values of B_α have been published [14,20]. The result of our measurement $B_\alpha = 0.016\pm0.005$ (see Fig. 10) is consistent with the average of the two previously published values. Since no experimental value for Γ_γ is available, the theoretical estimate from Ref. [20] was used to calculate the resonance strength $\omega\gamma$.

For higher-lying states, the resonance strengths from Ref. [20] were taken. The contribution of the direct reaction rate was calculated in Ref. [29] and predicted to be smaller than the resonant rate by two to three orders of magnitude. The individual contributions to the astrophysical reaction rates are shown in Fig. 11(a), emphasizing the dominance of the $3/2^+$ and $7/2^+$ states at temperatures below $T_9\sim0.7$. The total reaction rate is given by the thick solid line in Fig. 11(a). The ratio between the rates obtained from previous estimates and measurements to the current experiment in the temperature range critical to the nova environment ($T_9=0.1$–0.5) appears in Fig. 11(b). With the exception of the rate from Ref. [30], which is larger by about a factor of 1.5, all other rates are in agreement with the upper limits obtained in this experiment.

The influence of the ^{15}O$(\alpha,\gamma)^{19}$Ne reaction on the residence time of ^{15}O in various astrophysical environments is shown in Figs. 12(a)–12(c). The ''destruction rate'' λ_r at

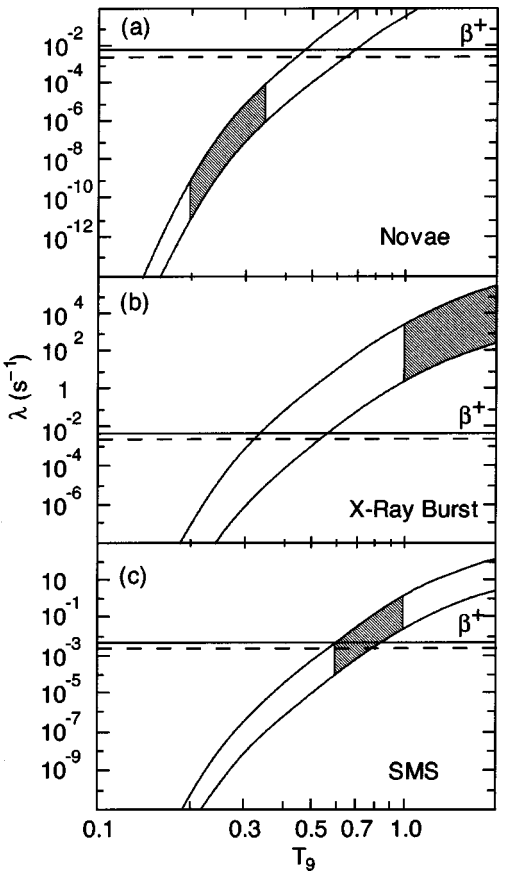

FIG. 12. Destruction rates of ^{15}O through the ^{15}O$(\alpha,\gamma)^{19}$Ne reaction as a function of the temperature T_9 in various astrophysical environments: (a) Novas, (b) x-ray bursts, and (c) supermassive stars. The gray areas are calculated from the reaction rates in Fig. 11(a) with different density-temperature regions given in the text. The solid horizontal line represents the β^+-decay rate of ^{15}O and the dashed line the CNO cycle rate (see text for details).

different astrophysical sites is obtained from the reaction rate $N_A\langle\sigma v\rangle$ through the equation

$$\lambda_r = \rho \frac{X}{A} N_A \langle \sigma v \rangle, \tag{3}$$

where ρ is the density in g/cm^3, X the mass fraction of the captured element, and A its mass number ($X=0.27$ and $A=4$ for ^{4}He). λ_r represents the average rate at which ^{15}O is destroyed in a particular astrophysical environment with density ρ and temperature T. Also shown by the two horizontal lines in Fig. 12 are the β^+ decay rate of ^{15}O ($\tau=177$ s, solid line) and the cycle rate of the CNO cycle ($\tau=279$ s, dashed line) which is dominated by the two waiting point nuclei ^{14,15}O. The conditions typical of novas explosions are shown in the λ-T plane in Fig. 12(a) ($\rho\sim10^2$–10^4 g/cm^3, $T_9\sim0.2$–0.35). From the marked area in Fig. 12(a), it can be seen that, even at extreme temperatures of $T_9\sim0.35$, the ^{15}O(α,γ) rate is still one to two orders of magnitude below the β^+ decay rate. How much of the CNO material is processed to ^{19}Ne and beyond during a nova explosion depends strongly on the duration of the thermonuclear runaway. The time window during which the temperature in a nova exceeds $T_9=0.1$ is about 500–1000 s [9,32], corresponding to about 2–4 CNO cycles. Because the destruction rate of ^{15}O via (α,γ) under nova conditions is several orders of magnitude smaller than the β^+ decay rate, no significant breakout towards heavier nuclei can be expected. This conclusion is confirmed by detailed calculations [9], where it is shown that at temperatures $T_9<0.3$, the amount of ^{22}Mg [produced via the sequence ^{15}O$(\alpha,\gamma)^{19}$Ne$(p,\gamma)^{20}$Na$(p,\gamma)^{21}$Mg$(\beta^+\nu_e)^{21}$Na$(p,\gamma)^{22}$Mg] is still three to five orders of magnitude below that of ^{14,15}O, indicating a negligible breakout probability via this route. For a significant breakout, temperatures above $T_9\geqslant0.6$ are required. Such temperatures are considerably higher than the peak temperatures predicted in typical nova models [9,32,33].

In contrast, the conditions in x-ray bursts [$\rho\sim10^3$–10^6 g/cm^3, $T_9\sim1$–2, see Fig. 12(b)] are such that the ^{15}O$(\alpha,\gamma)^{19}$Ne rate exceeds the β-decay rate by more than three orders of magnitude, indicating that, on the surface of a neutron star, ^{15}O is not a waiting point nucleus, but is easily processed towards heavier nuclei. The precise value of the α-decay branching ratio does not play a significant role in this environment.

Another astrophysical site where the breakout from the HCNO cycle might occur is in supermassive stars (SMSs), i.e., population III stars that potentially existed in the early stages of the universe. Their fate depends on the energy generated by hydrogen burning during the collapse phase. If enough energy is produced during this phase, the star might explode rather than collapsing into a black hole [31]. One of the reactions controlling the evolution of a SMS is, again, the breakout reaction ^{15}O$(\alpha,\gamma)^{19}$Ne. The ^{15}O destruction rate at this astrophysical site is shown in Fig. 12(c). In this environment, λ_r is comparable with the β decay rate of ^{15}O and, thus, a detailed knowledge of the resonance strength as well as of the temperature and density conditions in SMSs is crucial for predicting the fate of such objects.

V. CONCLUSIONS

A technique for measuring small branching ratios of particle-unbound states has been developed. It makes use of the kinematic focusing effects occurring in transfer reactions studied in inverse kinematics. By detecting in kinematic coincidence the heavy reaction products, which are produced with small yields in possible background reactions, very clean, background-free spectra are obtained. Because of the good particle identification and, consequently, low backgrounds it will be possible to measure branching ratios in the 10^{-5} range in sufficiently long experiments. The technique works best for states that are close to the energy thresholds, i.e., precisely the levels that dominate the astrophysical reaction rates. In the present case we studied the branching ratio of the 4.033 MeV $3/2^+$ state in ^{19}Ne, which was populated via the reaction ^{3}He$(^{20}$Ne$,\alpha)^{19}$Ne*(4.033). An upper limit $B_\alpha\leqslant6\times10^{-4}$ was obtained for this ratio. With this limit,

conclusions about the possible breakout from the hot CNO cycle into the rp process in novas, x-ray bursts, and supermassive stars were reached, indicating that the $^{15}O(\alpha,\gamma)^{19}Ne$ reaction does not provide a major breakout path for novas, but might have a strong effect on the fate of supermassive stars.

ACKNOWLEDGMENTS

This work was supported by the U.S. Department of Energy, Nuclear Physics Division, under Contract Nos. W-31-109-ENG-38(ANL) and DE-FG02-98ER-41086(NU) and by a NATO Collaborative Linkage Grant.

[1] A.E. Champagne and M. Wiescher, Annu. Rev. Nucl. Part. Sci. **42**, 39 (1992).
[2] R.K. Wallace and S.E. Woosley, Astrophys. J., Suppl. **45**, 389 (1981).
[3] C. Rolfs, Nucl. Phys. **A217**, 29 (1973).
[4] R. Morlock *et al.*, Phys. Rev. Lett. **79**, 3837 (1997).
[5] B. Harss *et al.*, Phys. Rev. Lett. **82**, 3964 (1999).
[6] B. Harss *et al.*, Phys. Rev. C **65**, 035803 (2002).
[7] J.C. Blackmon *et al.*, Nucl. Phys. **A688**, 142c (2001).
[8] K.E. Rehm *et al.*, Phys. Rev. C **55**, R566 (1997).
[9] M. Wiescher, J. Görres, and H. Schatz, J. Phys. G **25**, R133 (1999).
[10] L. Buchmann, TRIUMF Collaboration (private communication).
[11] D.R. Tilley, H.R. Weller, C.M. Cheves, and R.M. Chasteler, Nucl. Phys. **A595**, 1 (1995).
[12] Z.Q. Mao, H.T. Fortune, and A.G. Lacaze, Phys. Rev. C **53**, 1197 (1996).
[13] F. de Oliveira *et al.*, Phys. Rev. C **55**, 3149 (1997).
[14] P.V. Magnus, M.S. Smith, A.J. Howard, P.D. Parker, and A.E. Champagne, Nucl. Phys. **A506**, 332 (1990).
[15] S. Kubono *et al.*, Eur. Phys. J. A **13**, 217 (2002).
[16] A.M. Laird *et al.*, Nucl. Phys. **A688**, 134c (2001).
[17] J.D. Garrett, R. Middleton, and H.T. Fortune, Phys. Rev. C **2**, 1243 (1970).
[18] A. Wuosmaa (private communication).
[19] B. Fulton (private communication).
[20] B. Davids *et al.*, Phys. Rev. C **67**, 012801(R) (2003).
[21] Small c. m. angles in the following are defined as scattering from those collisions that result in minimum momentum transfers.
[22] W.N. Catford, D.M. Pringle, D.G. Lewis, A.E. Smith, E.F. Garman, I.F. Wright, and J. Lukasiak, Nucl. Instrum. Methods Phys. Res. A **247**, 367 (1986).
[23] J.C. Hardy, H. Brunnader, J. Cerny, and J. Jänecke, Phys. Rev. **183**, 854 (1969).
[24] J.W. Frickey, K.A. Eberhard, and R.H. Davis, Phys. Rev. C **4**, 434 (1971).
[25] D.R. Tilley, C.M. Cheves, J.H. Kelley, S. Raman, and H.R. Weller, Nucl. Phys. **A636**, 249 (1998).
[26] K.E. Rehm and F.L.H. Wolfs, Nucl. Instrum. Methods Phys. Res. A **273**, 262 (1988).
[27] I. Narsky, Nucl. Instrum. Methods Phys. Res. A **450**, 444 (2000).
[28] G. Hackman *et al.*, Phys. Rev. C **61**, 052801(R) (2000).
[29] K.H. Langanke, M. Wiescher, W.A. Fowler, and J. Görres, Astrophys. J. **301**, 629 (1986).
[30] R.K. Wallace and S.E. Woosley, Astrophys. J., Suppl. Ser. **45**, 389 (1981).
[31] G.M. Fuller *et al.*, Astrophys. J. **307**, 675 (1986).
[32] S. Starrfield, W.M. Sparks, J.W. Truran, and M.C. Wiescher, Astrophys. J., Suppl. Ser. **127**, 485 (2000).
[33] J. Jose, A. Coc, and M. Hernanz, Astrophys. J. **560**, 897 (2001).